75th International Astronautical Congress (IAC), Milan, Italy, 14-18 October 2024.

IAC-24-C4.IPB.15,x88178

Design of an Additively Manufactured Bipropellant Thruster for In-Orbit Satellite Operations

Davide Zuin[a], Simone La Luna[a], Michele Ianniello[a], Filippo Maggi[a]

[a] *Space Propulsion Laboratory (SPLab), Department of Aerospace Science and Technology (DAER), Politecnico di Milano, Via La Masa 34, 20156 Milan, Italy*
* Corresponding Author, davide.zuin@dorbit.space

Abstract

Within the last decade, the new space propulsion panorama has seen a rapid evolution, particularly concerning the manufacturing of thrust chambers for liquid rocket engines. The implementation of Selective Laser Melting for thrusters production has enabled the resolution of previous manufacturing constraints, thereby allowing innovative engineering solutions.

This study aims to outline the development and verification processes of a liquid rocket engine designed for low thrust and in-space operations. The engine is designed to utilize storable ‘green’ and self-pressurized propellants, addressing the issues associated to the implementation of harmful toxic propellants in space propulsion. The design concept of the engine leverages on the capabilities offered by Additive Manufacturing, allowing for the integration of multiple functionalities — such as the combustion chamber, nozzle, regenerative cooling channels, thermal slug, injection plate, and sensor housing — into a single build, in contrast to traditional liquid rocket engines that typically require numerous parts and mechanical connections. The work focuses on the design and optimization of regenerative cooling channels within the thrust chamber structure. Design alternatives are presented and a mathematical method for the parameterization of the inner channels is developed. The evaluation of the proposed models is carried out through a series of sample prints, each of which is subjected to a dedicated analysis via Non-Destructive Inspections methods. Relationships between the geometric modelling choices and the distances between channels and chamber, the assessment of channel circularity in light of printing challenges, and the quality of the surface finish in as-built conditions are recovered. The results of the sample prints comparison allow to refine the final engine design.

Keywords: Selective Laser Melting, Design for Additive Manufacturing, Green Propellants, Thruster Family, Regenerative Cooling, Computed Tomography

Acronyms/Abbreviations

AM	Additive Manufacturing
CAD	Computer Aided Design
CC	Combustion Chamber
CFD	Computational Fluid Dynamics
CT	Computed Tomography
DfAM	Design For Additive Manufacturing
FEM	Finite Element Analysis
EDX	Energy Dispersive X-ray Spectroscopy
FEM	Finite Element Method
LRE	Liquid Rocket Engine
MMH	Monomethyl Hydrazine
NDI	Non-Destructive Inspection
SEM	Scanning Electron Microscopy
SLM	Selective Laser Melting

1. Introduction

In the last decade, the new space economy has grown at an increasing pace, driving the technological progress and the quest for innovative engineering solutions for each one of the subsystems characterizing a satellite, including the propulsion segment. Within this framework, the upcoming new generation of in-space rocket propulsion engines aims to achieve two primary goals: exploring novel non-toxic, cost effective, storable liquid propellants for monopropellant and bipropellant systems and develop new engine designs which benefit of the potentialities offered by innovative metal Additive Manufacturing (AM) technologies, such as Selective Laser Melting (SLM).

1.1 ‘Green’ Propellants

Currently, one of the main trends in the space propulsion field revolves around the development of ‘green’ propellant alternatives for space propulsion applications [1]. The demand for better propellant performance (e.g., higher thrust or specific impulse) is gradually combined with other properties which can be considered the distinctive features of a ‘green’ propellant. These characteristics include: reduced health hazard risks both for propellant and exhaust flow species; environmental sustainability of the propellant; storage and handling cost reductions, and more [2]. The storability and specific impulse values of hydrazine and its derivatives, such as monomethyl hydrazine (MMH) and unsymmetrical dimethyl hydrazine (UDMH), have positioned them as top choices for rocket fuels. Nevertheless, the rising costs associated with handling of these toxic propellants have significantly increased. In 2011, hydrazine was included in the list of the Substances of Very High Concern by the framework legislation of the European Commission for the Registration, Evaluation, Authorization and Restriction of Chemicals (REACH), while MMH has been classified by the European CHemicals Agency (ECHA) as a possible carcinogenic substance [3]. Given these circumstances, the future availability and affordability of these propellants remain uncertain; this has led to a renewed industrial interest towards the research and development of new high-performance, cost-effective alternatives for hydrazine.

Among the solutions in "green" propellant subsystems, nitrous oxide (N_2O) based applications have rapidly become a prominent subject of study. These system are characterized by a minimal or non-toxic nature, self-pressurizing characteristics and high performance results [4]. As an example, the combination of N_2O with a light hydrocarbon, such as ethane (C_2H_6), exhibit a sufficiently high vapor pressure at room temperature which qualifies them for utilization as self-pressurized propellants, eliminating the need for extra components in a pressurization setup. The result allows for specific impulse values in vacuum above 280s [4]. Nitrous oxide based bipropellant system are characterized by further versatility characteristics, as premixed oxidizer-fuel blends or non-premixed solutions are possible. These systems allow the development of multi-mode solutions, where only one tank and one feeding system can be implemented in a monopropellant motor fashion [5] or in bipropellant configuration when adding a second fluidic line.

Despite these considerations, the integration of N_2O engines on satellites still presents different challenges. In particular, high flame temperatures produced during the combustion of the two substances remains a threat to the effective functioning of a thruster. As an example, within the research of Palacz et al., the use of N_2O in low-thrust rocket engines is analysed, revealing combustion flame temperatures for the combinations of N_2O /Ethanol and N_2O /Ethylene propellants that reached as high as 3000K and 3250K, respectively [6]. This drawback of the selected propellant necessitates the design of a suitable cooling system, which adds complexity to the design of the thruster. Regenerative cooling is the predominant approach utilized in bipropellant chambers to lower wall temperatures to within acceptable limits and prevent potential failure. This method involves circulating one of the propellants around the thruster body using suitable cooling channels [7]. Achieving an optimal cooling channels design requires a significant number of iterations involving various parameters, such as the quantity of channels, their shapes, cross-sections and the wall thicknesses in-between. It is a prevailing trend in this context that enhancing cooling performance is linked to an increase in the complexity of the channel design, prompting the investigation of new manufacturing technologies to manage this added complexity in a cost-effective manner.

1.2 Additive Manufacturing of Space Thrusters

Additive Manufacturing (AM) is taking the lead in the fabrication of high-profile applications within the aerospace framework due to its distinctive advantages, most notably the apparent unlimited design freedom it grants during the design phase. This peculiarity allows to reach an higher degree of complexity of designed parts, something which was not achieved by conventional manufacturing methods. Therefore, AM promotes the concept of "design for performance" rather than an approach tailored for the manufacturability of the final component [8].

In conjunction with the design flexibility, the need of processing materials with high-strength at elevated temperatures is key within thruster manufacturing. Ni-based superalloys like Inconel 718, Inconel 625, and Hastalloy X are considered state-of-the-art choices for such applications [9]. When considering this design constraint, AM Selective Laser Melting (SLM) stands out as the main option in meeting the demand compared to alternative technologies, as it enables the production of fully dense metal components using these materials with excellent mechanical properties and high precision [10, 11].

Despite the promoting characteristics of AM in thruster manufacturing, drawbacks of this technology are present which limit the widespread of AM in the industry. The apparent limitless freedom provided by SLM still presents some challenges by phenomena such as dross formation and powder adhesion [12]. Besides optimizing the process parameters, the primary measure to prevent or mitigate these critical issues potentially affecting the final product quality is to establish strict design regulations to control the process. The creation of design guidelines that define the printability limits of the machine is essential as it helps to prevent build failures and extra costs. Test prints that incorporate various basic design features and artifacts are present in literature [13, 14]. An example of test artifact for benchmarking activities is reported in Figure *1*. The target of these activities is the identification of manufacturability limits of each build features by varying specific geometrical parameters (e.g., wall thickness, inclination, other). After their identification through benchmarking activities, the critical geometrical features to be characterized are printed multiple times to evaluate machine

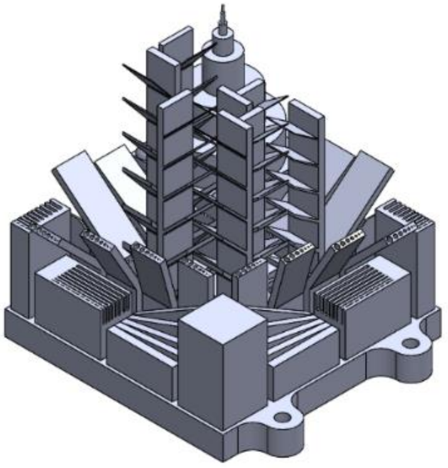

Figure 1: Example of test artifact CAD model. Courtesy of D-Orbit company.

characteristics and postprocessing activities. When considering in-space thrusters, critical characteristics usually include internal channels for the regenerative cooling and injector designs, thin walled structures for the divergent part of nozzles, overhangs and axisymmetric structures for the thrust chamber and main body.

1.3 Thruster family

When considering the development of in-space thrusters, a comprehensive technical background involving expertise in fluid dynamics, chemistry, heat transfer, material science, manufacturing processes, mechanical design, electronics, and other fields is necessary. Effective iterations and feedback among these disciplines are crucial in achieving an optimal design result. The significant amount of time and resources required to achieve this goal highlight the convenience of leveraging on rapid prototyping capabilities provided by AM. Furthermore, the concept of rapid prototyping allows for the development of different thruster classes in terms of thrust, where engines of the same family share same basic design concepts such as propellant and incorporate components that are either identical or slightly modified versions of the same type.

The design process associated to the “thruster family” leverages on the development of a base design of a thruster as initial step. After the first design is completed and tested, small engine characteristics modifications are introduced to generate a thruster with a different thrust class. Therefore, the new class capitalizes on previous hardware, software, test data, qualified vendors, technical and fabrication personnel, and occasionally, the use of debugged materials, fabrication, and test facilities from the previous engine class. This very often leads to reduced costs, accelerated achievement of high engine reliability, and frequently a shorter schedule and increased confidence from the developer/contractor [7].

Within this work, an overview of a thruster family is presented. The focus of the work will be centred on the iterations performed on the cooling channels of the thrusters in order to maximise the heat transfer during working conditions. The design of the channels are analysed considering the challenges provided by the AM SLM technology selected. Finally, a comparison of the various design, a cooling channel selection and future developments of the thruster class are presented.

2. Thruster Commonalities and Differences

The thruster family selected presents three main classes, which represent respectively the qualitative level of low, medium and high size and thrust. This family is manufactured with a set of core design principles: they all involve self-pressurized “green” nitrous oxide propellants to feed the system; they all implement regenerative cooling as the designated cooling strategy; they are all manufactured with a Ni-based superalloy material; they adopt AM SLM manufacturing technology; and they are developed with an high-level design concept in terms of thruster mechanical, electrical and fluidic interfaces emphasizing modularity and interchangeability on multiple platforms.

From this description, it is clear that the family of bipropellant thrusters is based on oxidizer N_2O: however, no restrictions in terms of fuel are introduced. The only constrain is associated to the requirement of self-pressurization of both propellants from a system perspective: this leads to the selection of fuels from the light hydrocarbon definition (propane, propene, ethylene, ethane, others). When considering these bipropellant combinations, high combustion flame temperature poses a risk of system failure. To address this concern, all engines are equipped with an integrated system of regenerative cooling channels. While traditional manufacturing methods used to limit the cost-effective fabrication to basic channel shapes [15], AM unlocks new opportunities that prioritize cooling performance over construction simplicity. Therefore, the engine family has been manufactured using a common SLM machine. This is of utmost importance, as variations in the SLM process across different machines can significantly impact the final quality of the product. Studies conducted on dedicated test artifacts, as the one presented in Figure *1*, allowed to find the optimal process parameters and define the design constraints for all the thruster classes within the family, in particular for what concerns the information on the minimum self-supporting angle, internal channels geometries, the geometrical tolerances and the surface roughness achievable [14].

The Design for Additive Manufacturing (DfAM) strategy for the three Liquid Rocket Engines (LREs) takes advantage of part consolidation design philosophy in order to integrate many functionalities in just one single component. Within the thrusters, the combustion chamber, the nozzle, the regenerative cooling channels, the thermal slug, the injection plate and the housing for different sensors are all combined in a single AM build. This effort allows to limit the number of parts from hundreds of components and mechanical joints in conventional LREs to a few dozens. As an intrinsic drawback of this approach, significant complexity is associated to the design step of an AM LRE of this type.

Another key aspect of the family is the emphasis on modularity within the three engine design, which allow the development of multiple thrust classes. The engines share the same footprint and interface plate design, as reported in Figure 2, enabling effortless interchangeability on a primary platform that supports the required fluidic, mechanical, and electronic interfaces.

3. Design to Verification

The description of the thruster development process can be structured in the following phases: design, parametrization, manufacturing and verification. The primary target of the work has been focused on the regenerative cooling channels of the engine with smaller thrust. Following the previous definition, this is the smallest engine within the designed family. Therefore, the result reports geometrical features which significantly challenge the manufacturing capabilities of a SLM machine, in particular regarding the internal channel diameters, inclinations and paths. Consequently, this thruster serves as an ideal case study to evaluate the potential of additive manufacturing SLM in its most demanding circumstances.

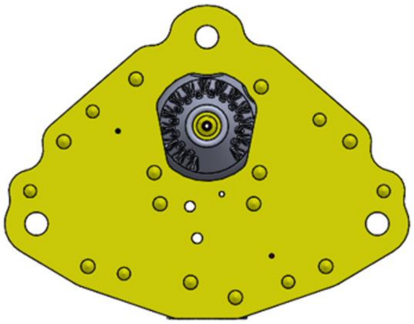

Figure 2: Example of AM thruster footprint, interface plate bottom view.

3.1 Design

The design phase primarily revolved around the regenerative cooling channels; the main design driver was based on the optimization of channels housed within the engine. Besides a conventional approach based on longitudinal channels along the thrust chamber, in this phase more exotic channels shapes were investigated: these included inclined and spiral configurations aimed at enhancing the cooling jacket effectiveness.

Few research studies are present on spiral channel regenerative cooling effectiveness for LREs. The study from Lv et al. reports that the application of the spiral channel significantly improves the cooling effect under the same channel size and boundary condition [16]. A partial manifestation of the improved cooling effect for the spiral channel is that the equivalent flow velocity in the spiral channel is faster than that of the straight channel, as it depicted in Figure *3*.

Within the reference, the equivalent flow per axial length of the spiral channel can be expressed as follows:

$$\dot{m}_1 = \dot{m}_2 / \cos\theta$$

Within the same time t, the total coolant mass through the spiral channel and the straight channel can be expressed as:

$$m = \rho A v t$$

So, according to the previous two equations, flow velocity reports:

$$v_1 = v_2 / \cos\theta$$

This means that when the distance between the coils of the helix (or pitch of the helicoidal pattern) is reduced, the angle θ in the velocity equation increases and the coolant velocity accelerates, resulting in a better cooling effect.

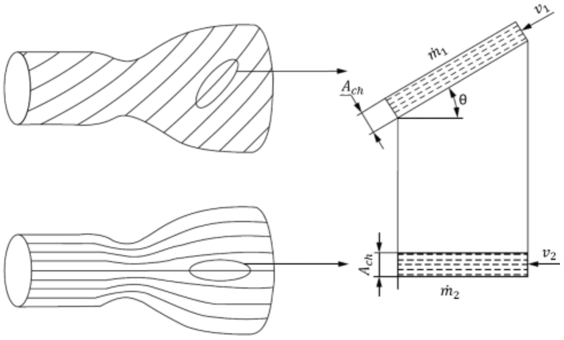

Figure 3: Spiral channel and straight channel schematics; adapted from [16].

The maximum angle θ_{max} that can be used in the application, corresponding to a geometrical maximization of the cooling flow path that can be reached, is limited by two main factors: the chemical stability of the regenerative fluid within the temperature range of operation; and the manufacturing capacity of the SLM machine.

Considering the first factor, if N_2O propellant is assumed as coolant within the regenerative cooling, the cooling performance is constrained by the maximum heat absorption capacity before the propellant undergoes decomposition into nitrogen and oxygen. If the oxidizer reaches its decomposition temperature of ~580 °C [17] prior to injection into the combustion chamber, this could lead to performance instabilities of the overall assembly. Therefore, propellant decomposition in the regenerative channels represents an intrinsic limitation of regenerative cooling within the selected thruster design. Simplified models and CFD simulations can be employed during the design phase to evaluate the maximum heat absorption capacity. However, these analyses exceed the scope of this research, therefore they will not be treated in this study.

When considering the manufacturability factor, the maximum inclination angle θ_{max} achievable with an acceptable level of surface roughness and geometric accuracy on a SLM machine for a given material is mainly influenced by the dimensions and cross-sectional geometry of the channel [18]. Within this work, a focus on the evaluation of these critical values has been performed through the development of a dedicated CAD parametrization of the regenerative channels and a sequent experimental test campaign.

3.2 Thruster CAD Parametrization

The thruster CAD model parametrization aimed to investigate novel design options for regenerative cooling channels to be then verified through dedicated test prints subjected to Non-Destructive Inspection (NDI) techniques. The output of this investigation allowed to identify the optimal cooling channel configuration, leading to the finalization of the thruster design and the final 3D-print of the complete device.

The study covered three different geometries for the regenerative cooling channels: spiral, longitudinal and zig-zag pattern, resulting in 27 different models where 9 models were allocated to each geometry. For the spiral and longitudinal channels, the design parameters selected were the channel cross section and the total number of channels integrated within the thruster body. Concerning the cross section, previous literature analyses on straight channels within SLM samples involving Ni-based alloys demonstrated that circular spiral channels could be manufactured successfully down to a diameter of 0.8 mm [18]. Therefore, within this parametrization study, it was considered reasonable to lower this cross-sectional limit for longitudinal channels to 0.6 mm. This assumption is corroborated by the work of Diegel et al., where it emerges that vertical channels are typically easier to print with respect to their inclined counterparts [12].

Regarding the zig-zag channels, after having fixed the cross section and the number of channels respectively to 0.9 mm x 1.1 mm and 12, a different parametrization approach has been selected. The selection was driven by the possibility to define the zig-zag pattern by selectively tuning the numerical parameters associated to a damped sine wave equation directly implemented on the CAD model. The wave was selected according to the following equation:

$$y = A \cdot e^{-\lambda x} \cdot \sin(\omega x)$$

The impact of the equation on the channel path shape is reported in Figure *4*. The selected wave equation reports three main parameters: the amplitude A, the damping factor λ and the angular frequency ω. The amplitude represents the highest peak of the wave, thus affecting the maximum inclination of the channel. The damping factor λ is responsible for the wave's decay rate, which in turn affects the sharpness of the inclination change from the engine's base to the throat. The angular frequency ω influences the channel's inclination as well, with increased values leading to more stringent manufacturing requirements for the channel.

The equation peculiarities allowed to define a sinusoidal function that includes a gradual reduction in amplitude as it nears the throat of the thruster. Such a design promotes increased versatility, with channels that are more steeply inclined in the convergent region to optimize the cooling effect, while the channels at the throat remain straighter, for structural and manufacturability reasons. In the equation, a damping factor of 0.06 was selected as constant variable while amplitude and angular frequency were considered as the two independent parameters. This selection allowed to retrieve 9 different models for the zig-zag pattern samples.

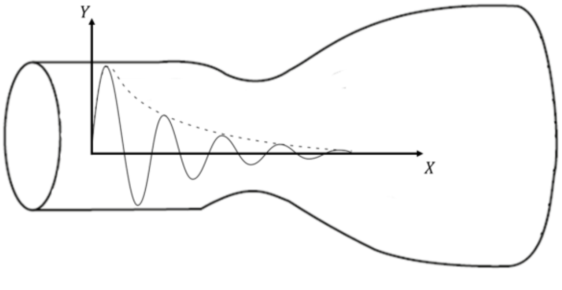

Figure 4: Zig-zag regenerative cooling channels definition.

Table 1: Spiral channel parametrization data.

Code	Cross Section [mm]	#Channels [-]
S-A1	0.9x1.1	11
S-A2	0.9x1.1	12
S-A3	0.9x1.1	13
S-B1	0.8x0.8	12
S-B2	0.8x0.8	13
S-B3	0.8x0.8	14
S-C1	1.1x1.3	10
S-C2	1.1x1.3	11
S-C3	1.1x1.3	12

Table 2: Longitudinal channels parametrization data.

Code	Cross Section [mm]	#Channels [-]
L-A1	0.9x1.1	12
L-A2	0.9x1.1	13
L-A3	0.9x1.1	14
L-B1	0.8x0.8	13
L-B2	0.8x0.8	14
L-B3	0.8x0.8	15
L-D1	0.6x0.6	14
L-D2	0.6x0.6	15
L-D3	0.6x0.6	16

Table 3: Zig-zag channels parametrization data.

Code	Amplitude	Angular Frequency
Z-A1	2.25	0.13
Z-A2	2.25	0.16
Z-A3	2.25	0.19
Z-B1	1.5	0.19
Z-B2	1.5	0.22
Z-B3	1.5	0.25
Z-C1	3	0.07
Z-C2	3	0.1
Z-C3	3	0.13

Figure 5: Thruster printed specimens: longitudinal, spiral and zig-zag samples are reported.

For cataloguing reasons, a mnemonic code was assigned to each model, with the initial letter representing the type of channel geometry: S for spiral, L for longitudinal, and Z for zig-zag. The parameters chosen for each model are presented in Table *1*, Table *2* and Table *3*.

3.3 Manufacturing

The 27 parametrization specimen were manufactured via SLM using "virgin" powder (without recycling) and with the same process parameters. All the samples were printed in a single printing job; a Concept Laser M2 series 3 machine with 400W laser was considered. No support structures were required for the print and the only postprocessing operations performed were the sample cutting from the build plate through a band saw and a sequent sample cleaning from the powder remnant of the SLM process by means of ultrasonic bath method.

As illustrated in Figure *5*, each specimen was limited to a portion of the complete thruster model. The selected section encompassed the features associated to the parametrization analysis, specifically the regenerative cooling channels around the thrust chamber. This approach was selected to maximize the number of specimens on the same machine building platform, to minimize costs and to avoid issues due to other thruster parts, such as interface plate or thruster divergent sections potentially affecting the parametrization results.

3.4 Verification

The main objective of the inspection and verification activity was to assess whether the convoluted regenerative cooling channels designs, as modelled in the CAD, could be effectively produced using SLM while maintaining an acceptable level of geometric deviation from their intended specifications. In particular, the study focused on the minimum wall thickness between the channels, the channels circularity and their surface finish.

A distinct measurement strategy was developed to analyse each one of these properties, incorporating Computed Tomography (CT) and ultimately relying on specific image processing algorithms applied to the CT-scans.

3.4.1 Minimum Wall Thickness

The primary properties to be assessed included the minimum distance between each pair of adjacent channels and the minimum distance from the channels to the combustion chamber. Upon opening the CT scan digital files through the dedicated software myVGL, these distances were measured using the built-in digital “caliper” tool: the surface determination algorithm implemented by the software, specifically the ISO50 method, was considered to recover the areas corresponding to the minimal distance between the parts of the thruster under analysis. For a given a specimen, measurements were taken at five uniformly spaced heights along its axis and for each channel present at that section, as reported in Figure *6*.

For each actual measurement retrieved with this method $x_{i,actual}$, the associated nominal value derived from the CAD model $x_{i,nominal}$ was subtracted to determine the nominal/actual geometrical deviation ε_i. To facilitate data management, especially given the large number of parametrizations, a global value was associated to each specimen computing a mean value $\bar{\varepsilon}$ over all the measurements N taken for that particular specimen:

$$\varepsilon_i = x_{i,actual} - x_{i,nominal}$$

$$\bar{\bar{\varepsilon}} = \frac{1}{N}\sum_{i=1}^{N} \varepsilon_i$$

The associated standard deviation S and the standard error S_ε were computed as follows:

$$S = \sqrt{\frac{1}{N-1}\sum_{i=1}^{N}(\varepsilon_i - \bar{\bar{\varepsilon}})^2}$$

$$S_{\bar{\varepsilon}} = \frac{S}{\sqrt{N}}$$

3.4.2 Channels Circularity

The circularity of the channels was determined through a dedicated Matlab script, specifically developed for the purpose.

The image postprocessing performed by the code is graphically reported in Figure *7*. After exporting the greyscale image of the channel from myVGL software into Matlab, the script executes a series of image processing tasks. Initially, a binary image is created by converting all pixel values exceeding a globally established threshold to ones (corresponding to colour white), while all other values are set to zeros (corresponding to colour black). The threshold value is computed using the Otsu's method, which relies on the minimization between class variance for the background and foreground [19, 20].

Subsequently, the image undergoes a cleaning process to eliminate any potential porosity or image defect surrounding the actual channel. This is performed by discarding all objects made up of fewer than a specified number of pixels within the original binary image. The threshold value is iteratively adjusted until a satisfactory clean image is achieved.

At this point, an hole filling operation is performed to ensure that no white pixel are left inside the channel perimeter. This operation is performed through an in-built Matlab function which leverages on a morphological reconstruction based algorithm [21, 22]. The exterior boundaries of the channel are then delineated with another in-built Matlab function which implements the Moore-Neighbor tracing algorithm modified by Jacob's stopping criteria [23, 24].

Ultimately, the circularity of the channel ϕ can be evaluated using the following geometrical definition:

$$\phi = \frac{4\pi A}{P^2} \cdot \left(1 - \frac{0.5}{R_{eq}}\right)^2$$

where A and P are respectively the channel's area and perimeter, while the equivalent radius R_{eq} is defined as:

$$R_{eq} = P/(2\pi) + 0.5$$

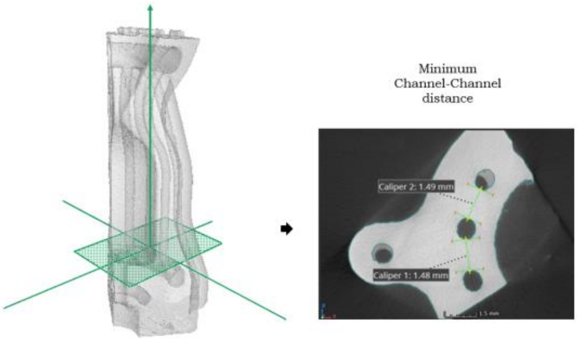

Figure 6: Example of minimum wall thickness measurement strategy.

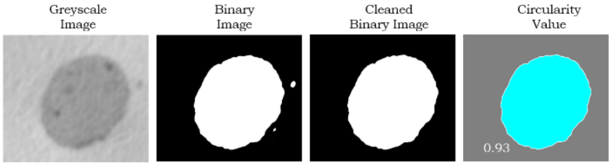

Figure 7: Example of channel image processing operations.

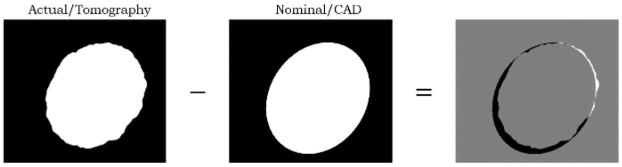

Figure 8: Example of image subtraction postprocessing.

This value is used to calculate a correction factor in order to avoid that the code returns values greater than 1. The maximum circularity value, corresponding to 1, is associated to an ideal circular shape; however it could be exceeded if the region is fuzzy or not perfectly convex [25].

Finally, to evaluate the nominal and actual geometrical deviation for each channel, the circularity measurement is compared to its nominal value obtained from the CAD. Following this comparison, a mean value and the corresponding standard error for each specimen are calculated in accordance with the methodology described in Section 3.4.1.

3.4.3 Channels Surface Irregularity

The surface irregularity of the channels is retrieved through another dedicated Matlab script. The code takes in input two greyscale images: one depicting the actual channel as captured by the CT-scan and the other representing the nominal channel as defined on the CAD. The first basic image processing operations performed on the two images are the same reported in Section 3.4.2. Once two clear binary images are obtained, the nominal channel image is subtracted from the actual channel image, resulting in a new image where the pixel values represent the difference between the corresponding pixels of the two images. Since this operation is performed on binary images, the pixels of the resulting image can only assume three distinct values: -1 (corresponding to colour black) for pixels that are situated outside the channel perimeter in the actual channel image but within the channel perimeter in the nominal image; 1 (corresponding to colour white) for pixels that are found inside the channel perimeter in the actual image yet outside the perimeter in the nominal image; and 0 (corresponding to colour grey) for all other scenarios.

Considering the example reported in Figure *8*, the channels surface irregularity can be estimated as the average deviation of the actual profile from the nominal one. This calculation involves determining the total number of white pixels $\#P_W$ and black pixels $\#P_B$, which can be converted into an area using a conversion factor based on the scale indicated in the software, and then divide the resulting value by the nominal channel perimeter p_n:

$$SI = \frac{\#P_W + \#P_B}{p_n}$$

The defined surface irregularity parameter SI includes all the possible contributions causing the actual surface to deviate from the nominal one, namely surface roughness, waviness and other possible local flaws.

4. Results

The overall numerical results of the aforementioned analyses are summarised in Table 4, Table 5 and Table 6. Within each table, the nominal/actual geometrical deviation in terms of minimum channel-channel (ch-ch) distance, minimum channel-combustion chamber (ch-CC) distance, circularity ϕ and surface irregularity SI are reported for each specimen respectively.

Some comments on the results are possible, starting from the results retrieved for the thruster spiral channel specimens which are summarized in Table 4. As it can be noticed, the B type channels exhibited the worst results both in terms of geometrical accuracy and surface quality. This is probably caused by the fact that B type channels are characterized by a circular cross section, contrarily to A and C specimen which adopt an elliptical one. This observation aligns with the framework presented in DfAM guideline references, which indicate that while circular holes can be effectively constructed in a vertical orientation, it is preferable to use self-supporting geometries like elliptical shapes for inclined channels [12].

The results did not show any specific correlation between the number of channels and the geometrical error. This result highlights the potential of SLM technology in building denser pattern of small convoluted channels. Overall, the geometrical inaccuracy regarding the minimum distance can be considered acceptable for all specimens, as they fall within a range of 0.1 mm.

Table 4: Thruster spiral channels specimen results.

Code	ch-ch [mm]	ch-CC [mm]	ϕ [-]	SI [µm]
S-A1	0.063 ± 0.011	0.032 ± 0.006	-0.072 ± 0.02	45 ± 1
S-A2	0.094 ± 0.007	0.052 ± 0.004	-0.07 ± 0.021	45 ± 3
S-A3	0.085 ± 0.013	0.043 ± 0.007	-0.084 ± 0.031	40 ± 1
S-B1	0.126 ± 0.015	0.036 ± 0.006	-0.038 ± 0.012	53 ± 2
S-B2	0.157 ± 0.014	0.055 ± 0.01	-0.04 ± 0.011	50 ± 1
S-B3	0.152 ± 0.014	0.049 ± 0.007	-0.002 ± 0.006	49 ± 1
S-C1	0.08 ± 0.013	0.021 ± 0.009	-0.092 ± 0.02	43 ± 4
S-C2	0.095 ± 0.010	0.039 ± 0.006	-0.05 ± 0.021	46 ± 4
S-C3	0.046 ± 0.016	0.038 ± 0.006	-0.052 ± 0.022	37 ± 3

Table 5: Thruster longitudinal channels specimen results.

Code	ch-ch [mm]	ch-CC [mm]	ϕ [-]	SI [μm]
L-A1	0.058 ± 0.012	0.029 ± 0.01	-0.128 ± 0.026	36 ± 4
L-A2	0.061 ± 0.007	0.032 ± 0.011	-0.036 ± 0.008	48 ± 3
L-A3	0.066 ± 0.005	0.029 ± 0.007	-0.026 ± 0.005	35 ± 3
L-B1	0.053 ± 0.008	0.049 ± 0.008	-0.054 ± 0.007	37 ± 4
L-B2	0.049 ± 0.007	0.039 ± 0.01	-0.048 ± 0.002	34 ± 4
L-B3	0.059 ± 0.004	0.032 ± 0.007	-0.026 ± 0.01	39 ± 2
L-D1	0.075 ± 0.009	0.065 ± 0.01	-0.086 ± 0.021	48 ± 4
L-D2	0.078 ± 0.009	0.061 ± 0.011	-0.1 ± 0.038	48 ± 5
L-D3	0.075 ± 0.004	0.071 ± 0.01	-0.052 ± 0.013	48 ± 5

Table 6: Thruster zig-zag channels specimen results.

Code	ch-ch [mm]	ch-CC [mm]	ϕ [-]	SI [μm]
Z-A1	0.096 ± 0.012	0.053 ± 0.017	-0.082 ± 0.021	42 ± 4
Z-A2	0.111 ± 0.022	0.03 ± 0.014	-0.156 ± 0.047	47 ± 6
Z-A3	0.161 ± 0.029	0.041 ± 0.01	-0.118 ± 0.024	61 ± 3
Z-B1	0.097 ± 0.02	0.028 ± 0.01	-0.05 ± 0.014	46 ± 5
Z-B2	0.178 ± 0.048	0.014 ± 0.013	-0.088 ± 0.018	52 ± 3
Z-B3	0.16 ± 0.034	0.03 ± 0.007	-0.088 ± 0.027	53 ± 8
Z-C1	0.091 ± 0.012	0.048 ± 0.014	-0.058 ± 0.012	46 ± 3
Z-C2	0.123 ± 0.012	0.044 ± 0.007	-0.062 ± 0.022	53 ± 3
Z-C3	0.149 ± 0.023	0.053 ± 0.015	-0.042 ± 0.013	45 ± 3

The measurements obtained from the thruster longitudinal parametrization reported reveal additional aspects. Longitudinal specimens exhibit enhanced geometrical accuracy and surface finish results. This output is in line with preliminary expectations, as vertical channels are generally simpler to fabricate with respect to their spiral counterparts. However, due to the same reason, it can be noticed that the benefits associated with self-supporting geometries are diminished. This can be highlighted when comparing A and B type specimen, as no significant difference between their results is reported in this case.

Looking at the values presented in Table 5, it becomes evident that the D type channels, which features a circular cross-section of 0.6 mm, represents the most critical design. Notably, despite its small size, the actual channels displayed a tendency to be undersized relative to their nominal dimensions, as illustrated in Figure 11. This behaviour has been observed consistently across all specimens, as evidenced by the positive values of all nominal and actual distancing deviations. This indicates an excess of dense material compared to expectations.

This phenomenon is particularly pronounced in smaller channels, where reductions of up to 40% relative to the nominal cross-sectional area have been recorded in the D3 specimen.

Finally, for what concerns the zig-zag specimen, the results reported in Table 6 were obtained. Among the zig-zag channel specimens, the Z-A3, Z-B2 and Z-B3 are the ones that exhibit the most significant deviations from their nominal geometries. This is primarily due to the low inclination of the channels imposed by the high angular frequency characterizing the damped sine wave defining the channel path (as described in Section 3.2). Additionally, the measurements taken on the Z-B3 specimen reveal an high standard error, indicating that the geometrical accuracy varies considerably along the channel and it is influenced by its local inclination.

Overall, the zig-zag channel specimens display the poorest geometrical accuracy. It is worth noticing that this is manifested only for the channel-channel distance, while the values obtained for the channel-combustion chamber distance are consistent with that of longitudinal and spiral specimens.

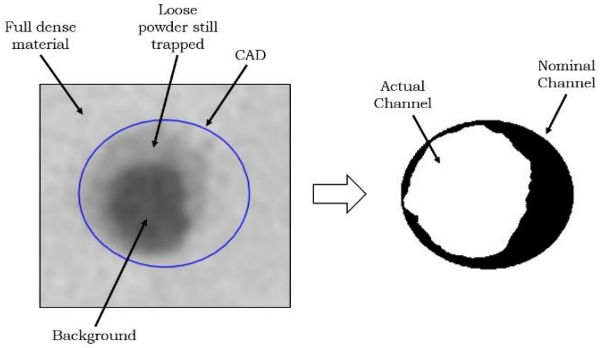

Figure 9: L-D3 specimen internal channel. Excess material in the channel is highlighted.

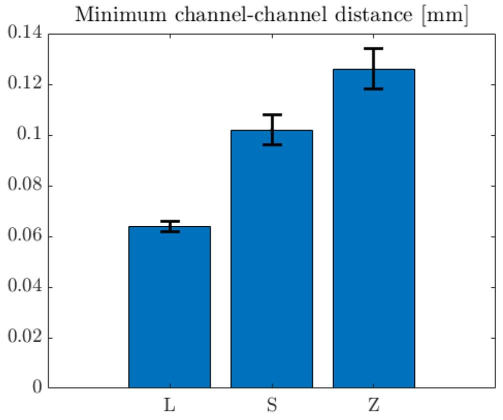

Figure 10: Minimum channel-channel distance: results comparison between L, S and Z specimens.

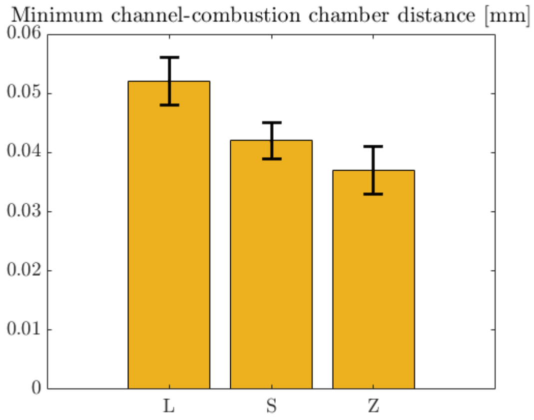

Figure 11: Minimum channel-CC distance: results comparison between L, S and Z specimens.

This phenomenon likely occurs because this parameter is not detrimentally influenced by the zig-zag design but is rather associated with the channel's inclination dictated by the engine's contour profile.

This hypothesis can be further validated by computing the mean and standard error of the pooled data set for each channel design type (L, S, and Z) and conducting a comparative analysis based on the four specified geometrical parameters (channel-channel distance, channel-combustion chamber distance, circularity and surface irregularity). The outcomes of this analysis are reported in Figure *10*, Figure *11*, Figure *12* and Figure *13* for the four descriptors respectively. Looking at the circularity parameter in the graph, it is possible to notice that the spiral channels achieved slightly better results. This is probably due to the fact that for the longitudinal channels parametrization, most of the nominal cross sections considered were all perfectly circular, rather than elliptical, so with a unitary circularity value that is hardly achievable.

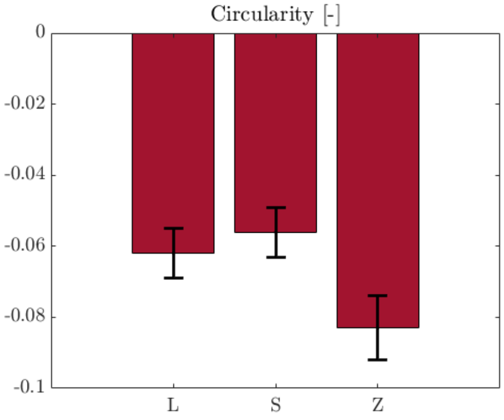

Figure 12: Channel circularity: results comparison between L, S and Z specimens.

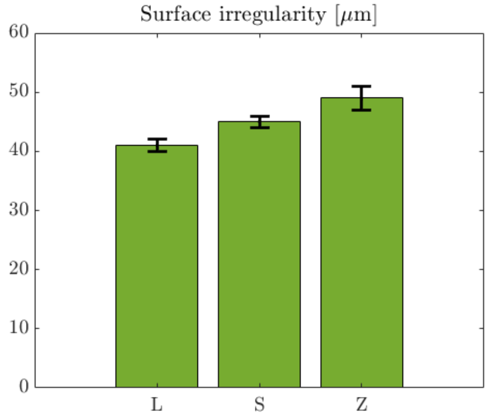

Figure 13: Channel surface irregularity: results comparison between L, S and Z specimens.

Another significant finding from the CT-scan is related to the quantity of powder that remained trapped in the specimen, that allows to determine the internal channels configuration that are more susceptible to powder entrapment in their as-built state.

The analysis revealed that longitudinal channels are less likely to retain powder compared to zig-zag channels; for instance, as reported in Figure *14*, sample L-A3 exhibited no evidence of trapped powder. However, D type longitudinal channels were entirely obstructed due to powder adhesion phenomena caused by the small diameter of the circular cross-section (nominally 0.6 mm), aligning with the results reported in the existing literature on the topic [26].

The quantity of powder retained within the zig-zag channels appears to be primarily associated with the angular frequency of the damped sine wave that delineates the channel's path. Specifically, at lower frequencies, the channels exhibit only partial obstruction due to the powder. Conversely, as the angular frequency rises, there is a marked increase in

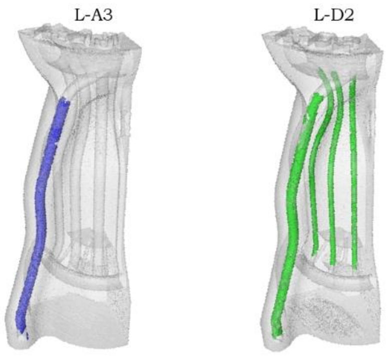

Figure 14: Powder trapped inside the L-A3 (left) and L-D2 (right) specimen.

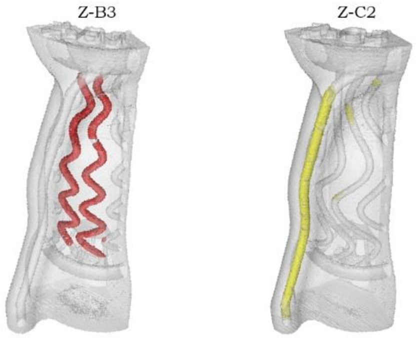

Figure 15: Powder trapped inside the Z-B3 (left) and Z-C2 (right) specimen.

the amount of powder accumulated, as illustrated in Figure *15*.

5. Comments

In order to support the thruster design phase, it is possible to embed the results presented in the earlier section within the decision-making process framework through the application of a selection matrix. The selection matrix is built assigning to each specimen a score related to its manufacturability and ranking them accordingly to this value. Referring to Tables 4 – 6, the nominal/actual geometrical deviation in terms of minimum channel-channel distance, minimum channel-combustion chamber distance, and surface irregularity are used to calculate a final score S for each specimen i as follows:

$$S_i = (ch - ch)_i + (ch - CC)_i + \mathrm{SI}_i$$

A partial ranking of the specimen is presented in Table *7*, where the best and the worst specimen for each parametrization type (S, L and Z) is reported.

Table 7: Overall specimen ranking considering the score S_i.

Rank	Specimen [-]	Score S_i [mm]
1	S-C3	0.121
2	L-B2	0.122
⋮	⋮	⋮
11	Z-B1	0.171
⋮	⋮	⋮
19	L-D3	0.194
⋮	⋮	⋮
26	S-B2	0.262
27	Z-A3	0.263

Consistently with the results presented in Chapter 4, the specimens that received the highest rankings overall are the ones featuring longitudinal channels. Notably, the L-B2 specimen, which integrates 14 channels with a circular cross section with a 0.8mm diameter achieved the second highest rank.

Nevertheless, some specimen characterized by spiral and zig-zag channels exhibited noticeable results even if they feature more inclined channels, in particular the S-C3 and Z-B1 models. Regarding the S-C3 specimen, its high ranking can likely be attributed to the utilization of a slightly larger elliptical cross-section (1.1 mm x 1.3 mm) which limits the detrimental effect of powder accumulation in the channels during the printing process. Conversely, the Z-B1 specimen score can be explained looking at the amplitude and frequency values characterizing the equation governing its channels. These values are the lowest selected for the zig-zag parametrization, leading to a less steep channels inclination.

These results demonstrate that the print inaccuracies of the internal channels caused by a greater angle relative to the building direction, can be mitigated to some degree through the implementation of elliptical cross-sections. This approach allows for the utilization of more intricate and potentially cooling-efficient channel configurations without compromising significantly the geometric precision [18]. Moreover, the ranking derived from this analysis may serve as a basis for a subsequent iteration aimed at combining different design parameters and refine the channel geometries to develop better ones. For instance, investigating zig-zag channels characterized by bigger elliptical cross-sections.

6. Conclusions and Future Developments

This work has presented a dedicated development and verification process of a LRE designed for low thrust and in-space operations utilizing ‘green’ propellants and self-pressurizing N_2O. An engine family with three separate classes has been defined, leveraging on AM SLM manufacturing technology. A dedicated parametrization associated to the cooling jacket channels within the thrusters has been presented, involving a design of experiment and multiple samples with three different inner geometries of regenerative channel designs. After tailored NDIs of each sample, a series of postprocessing operations has allowed to recover the criticalities in terms of specific descriptors, namely inner channel surface irregularity, circularity and specific distances between reference surfaces. The experiment allowed to define a ranking of the samples based on the aforementioned descriptors.

The ranking reported in Table 7 supports the identification process of the optimal channel geometry from a manufacturing perspective. It is necessary, however, to complement this with insights from other fields, for instance with the execution of preliminary Computational Fluid Dynamics (CFD) and Finite Element Method (FEM) simulation. After evaluating all pertinent aspects, including manufacturability, structural integrity, thermal performance, and cost, it becomes feasible to consolidate these elements into a comprehensive decision matrix. This matrix allows for the ranking of various designs, ensuring that only the most viable options proceed to the fabrication stage. Therefore, dedicated test prints and design of experiments, CFD, FEM and other computational tools allow to filter the samples which are the most promising enabling prompt adjustments to engine design, in conjunction with the rapid production capabilities of additive manufacturing. This approach leads to a robust strategy for iterative thruster design. The definition of the aforementioned decision scheme shall be integrated with a tailored qualification effort. Critical aspects associated to additively manufactured components intended for space applications shall be specifically addressed. First, cleanliness of a specimen necessitate further assessment, as specific techniques and procedures for SLM components cleaning and verification is mandatory. This characteristic significantly influences the design of a thrust chamber: from literature, suggestions include internal channels or cavities embedded with exits that enable the removal of residual powder and facilitate direct inspection whenever feasible [12]. Material analyses follow, such as mechanical, microstructural and chemical analyses. The manufacturing process for metal parts via SLM involves a complex thermal cycle, marked by repeated melting and rapid solidification, which affects significantly the mechanical properties of final components. Finally, a standardized approach towards testing is lacking, as various institutions and system manufacturers have developed their own methodologies and guidelines. A study conducted by Spierings et al. investigated the accuracy of three density measurement principles for additively manufactured metal components: Archimedes method, Micrograph of a cross-section and X-ray scanning. The Archimedes method showed a very high accuracy and repeatability, besides being very easy to use, fast and economic [27]. Quantification and characterization of all internal defects present in the product is therefore mandatory. The presence of complex geometries poses significant challenges, often rendering conventional testing methods ineffective for assessing pores, voids, and volumetric defects in the final product.

A clear design iteration scheme, coupled with a robust qualification framework would enable decision-makers involved in the development process to align their work more closely with qualification objectives, facilitating the creation of a comprehensive decision matrix for in-space thruster design and manufacturing and accelerating the overall product development process.

Acknowledgements

The authors want to acknowledge D-Orbit SpA and Sòphia High Tech srl for providing the machines and materials involved in this study.

References

[1] Marshall, W., Cavender, D., Maynard, A., & Zuttarelli, P. (2020). State of the Art in Green Propulsion-2020. *In-Space Chemical Propulsion TIM.*

[2] Ciezki, H. K. et al. (2019). Advanced Propellants for Space Propulsion - A Task within the DLR Interdisciplinary Project "Future Fuels". In *Proceedings of the 8th European Conference for Aeronautics and Space Sciences. (EUCASS)*. doi: 10.13009/EUCASS2019-276

[3] Mayer, A., & Wieling, W. (2018). Green propulsion research at TNO the Netherlands. *Transactions on aerospace research*, *2018*(4), 1-24. doi: 10.2478/tar-2018-0026

[4] Powell, O., Miller, J., Dreyer, C., & Papas, P. (2008). Characterization of hydrocarbon/nitrous oxide propellant combinations. In *46th AIAA Aerospace Sciences Meeting and Exhibit* (p. 999). doi: 10.2514/6.2008-999

[5] Pregger, T., Schiller, G., Cebulla, F., Dietrich, R. U., Maier, S., Thess, A., ... & Aigner, M. (2019). Future fuels—Analyses of the future prospects of renewable synthetic fuels. *Energies*, *13*(1), 138. doi: 10.3390/en13010138

[6] Palacz, T. (2017). Nitrous oxide application for low-thrust and low-cost liquid rocket engine. *Proceedings of the 7th EUCASS, Milano, Italy*, 3-6. doi: 10.13009/EUCASS2017-474

[7] Sutton, G. P., & Biblarz, O. (2017). *Rocket propulsion elements*. John Wiley & Sons, 9th edition.

[8] Buchbinder, D., Schleifenbaum, H., Heidrich, S., Meiners, W., & Bültmann, J. J. P. P. (2011). High power selective laser melting (HP SLM) of aluminum parts. *Physics Procedia*, *12*, 271-278. doi: 10.1016/j.phpro.2011.03.035

[9] Gradl, P., Tinker, D. C., Park, A., Mireles, O. R., Garcia, M., Wilkerson, R., & Mckinney, C. (2022). Robust metal additive manufacturing process selection and development for aerospace components. *Journal of Materials Engineering and Performance*, *31*(8), 6013-6044. doi: 10.1007/s11665-022-06850-0

[10] Herzog, D., Seyda, V., Wycisk, E., & Emmelmann, C. (2016). Additive manufacturing of metals. *Acta Materialia*, *117*, 371-392. doi: 10.1016/j.actamat.2016.07.019

[11] Kumar, M. B., & Sathiya, P. (2021). Methods and materials for additive manufacturing: A critical review on advancements and challenges. *Thin-Walled Structures*, *159*, 107228. doi: 10.1016/j.tws.2020.107228

[12] Diegel, O., Nordin, A., & Motte, D. (2020). *A practical guide to design for additive manufacturing* (p. 226). New York, NY, USA: Springer.

[13] Taylor, H. C., Garibay, E. A., & Wicker, R. B. (2021). Toward a common laser powder bed fusion qualification test artifact. *Additive Manufacturing*, *39*, 101803.

[14] Gradl, P. R., Tinker, D. C., Ivester, J., Skinner, S. W., Teasley, T., & Bili, J. L. (2021). Geometric feature reproducibility for laser powder bed fusion (L-PBF) additive manufacturing with Inconel 718. *Additive Manufacturing*, *47*, 102305.

[15] Pizzarelli, M. (2017). Regenerative cooling of liquid rocket engine thrust chambers. *Roma: Agenzia Spaziale Italiana (ASI)*. doi: 10.13140/RG.2.2.30668.92804

[16] Lv, J., Du, G., Jin, P., & Li, R. (2023). Heat Transfer Analysis and Structural Optimization for Spiral Channel Regenerative Cooling Thrust Chamber. *International Journal of Aerospace Engineering*, *2023*(1), 8628107. doi: 10.1155/2023/8628107

[17] Karabeyoglu, A., Dyer, J., Stevens, J., & Cantwell, B. (2008, July). Modeling of N2O decomposition events. In *44th AIAA/ASME/SAE/ASEE Joint Propulsion Conference & Exhibit* (p. 4933). doi: 10.2514/6.2008-4933

[18] Kasperovich, G., Becker, R., Artzt, K., Barriobero - Vila, P., Requena, G., & Haubrich, J. (2021). The effect of build direction and geometric optimization in laser powder bed fusion of Inconel 718 structures with internal channels. *Materials & Design*, *207*, 109858. doi: 10.1016/j.matdes.2021.109858

[19] Yang, X., Sun, W., & Giusca, C. L. (2022). An automated surface determination approach for computed tomography. *NDT & E International*, *131*, 102697. doi: 10.1016/j.ndteint.2022.102697.

[20] MathWorks. Imbinarize: Binarize 2-D grayscale image or 3-D volume by thresholding. URL: Binarize 2-D grayscale image or 3-D volume by thresholding - MATLAB imbinarize - MathWorks Italia. Last accessed 16th August 2024

[21] MathWorks. Imfll: Fill image regions and holes. URL: Fill image regions and holes - MATLAB imfill - MathWorks Italia. Last accessed 16th August 2024

[22] Soille, P. (1999). *Morphological image analysis: principles and applications*, Vol. 2, No. 3, pp. 170-171. Berlin: Springer.

[23] MathWorks. Bwboundaries: Trace object boundaries in binary image. URL: Trace object boundaries in binary image - MATLAB bwboundaries - MathWorks Italia. Last accessed 16th August 2024

[24] R. C. Gonzalez, R. E. Woods, S. L. Eddins. Digital Image Processing Using MATLAB. Prentice Hall, 2004.

[25] MathWorks. Regionprops: Measure properties of image regions. URL: Measure properties of image regions - MATLAB regionprops - MathWorks Italia. Last accessed 16th August 2024

[26] Sommer, D., Götzendorfer, B., Esen, C., & Hellmann, R. (2021). Design rules for hybrid additive manufacturing combining selective laser melting and micromilling. *Materials*, *14*(19), 5753. doi: 10.3390/ma14195753

[27] Spierings, A. B., Schneider, M. U., & Eggenberger, R. J. R. P. J. (2011). Comparison of density measurement techniques for additive manufactured metallic parts. *Rapid Prototyping Journal*, *17*(5), 380-386.
doi: 10.1108/13552541111156504.